Article

Emergent continuous time crystal in dissipative quantum spin system without driving

Check for updates

Shu Yang [1,2], Zeqing Wang [2,3,4], Libin Fu [1] ✉ & Jianwen Jie [2] ✉

Time crystals are a nonequilibrium phase of matter that extend fundamental spontaneous symmetry breaking into the temporal dimension, typically requiring external driving for their realization. Here, we explore the nonequilibrium phase diagram of a two-dimensional dissipative Heisenberg spin system without external coherent or incoherent driving. Through numerical analysis of spin dynamics, we identify nonstationary steady states, some of which are limit cycles with persistent periodic oscillations, while others exhibit chaotic, aperiodic behavior. The emergence of limit cycle steady states breaks the continuous time-translation symmetry of this time-independent many-body system, classifying them as continuous time crystals. We further validate these oscillatory behaviors by testing their stability against local perturbations and assess the robustness of the emergent continuous time crystals by introducing isotropic Gaussian white noise. This work provides insights into the intricate interplay between the dissipation and spin interaction, and opens possibilities for realizing dissipation-induced, heating-immune time crystals.

A time crystal (TC) is a phase of matter in which time-translation symmetry is spontaneously broken, and this spontaneous breaking manifests as persistent periodic oscillations in local physical quantities that are not inherent to the system's properties. This concept was originally proposed by Frank Wilczek as a phenomenon that spontaneously breaks time-translation symmetry in the ground or equilibrium state[1–4]. Although this idea was later negated by a series of rigorous no-go theorems[5–7], which ruled out the possibility of TCs in closed quantum systems with only short-range interactions[8], the introduction of time-dependent periodic coherent driving has enabled the realization of discrete time-translation symmetry breaking in nonequilibrium setups[9–11]. This phenomenon, known as Floquet time crystal or discrete time crystal[12–21], is characterized by a subharmonic response to the driving frequency and has been experimentally demonstrated in various systems[22–24], such as trapped-ions[25,26] and superconducting qubits[27]. Its key challenge remains the heating-induced limited lifetime, despite the proposal of mechanisms[26,28–31] such as many-body localization[27,32], prethermalization[26,28–31], and dissipation[19,28], which aim to slow down thermalization.

Dissipation has been shown to serve as a resource for performing quantum tasks[33–40]. For instance, by carefully designing dissipation to compete with coherent driving[41–48], or by engineering competition among dissipative processes, including incoherent driving[49], one can achieve dissipative time crystals. By transforming to a suitable rotating frame where the time-dependent aspect of the driving is eliminated, the system can exhibit a continuous time crystal (CTC) characterized by the spontaneous breaking of continuous time-translation symmetry[50–57]. These dissipative time crystals have been experimentally observed in various systems[58–66]. A perfect time crystal should exhibit an infinite lifetime[67–70], characterized by a robust never-ending oscillatory (OSC) behavior. This mathematically corresponds to a stable closed trajectory in phase space, defined as a limit cycle (LC), a core element in nonlinear dynamical phenomena[71], such as in grid power dynamics[72], circadian clocks[73] and quantum synchronization[74–81]. LCs are a broader concept than TCs; they do not require the system to be either a single-body or a many-body system, nor do they necessarily imply the breaking of time-translation symmetry. The quest for nonequilibrium states and phases[82–107] that include OSC phases[98–108] is a fundamentally important task in physics, predating TCs.

To the best of our knowledge, all systems exhibiting time crystal behavior are subjected to external driving, whether it be Floquet-driven[9–19], incoherent-driven[49], or driven-dissipative[41,42,42–46,50–66] scenarios. However, external driving not only introduces complexity to the real system but also raises concerns about heating. Moreover, the presence of driving

[1]Graduate School of China Academy of Engineering Physics, Beijing, 100193, China. [2]Shenzhen Key Laboratory of Ultraintense Laser and Advanced Material Technology, Center for Intense Laser Application Technology, and College of Engineering Physics, Shenzhen Technology University, Shenzhen, 518118, China. [3]Quantum Science Center of Guangdong-Hongkong-Macao Greater Bay Area (Guangdong), Shenzhen, 518045, China. [4]Department of Physics, Renmin University of China, Beijing, 100872, China. ✉e-mail: lbfu@gscaep.ac.cn; Jianwen.Jie1990@gmail.com

complicates the discernment of the contributions of other factors, such as interaction and dissipation, to the OSC behavior. Therefore, a fundamental question arises: Can a purely dissipative quantum system, without external coherent or incoherent driving, exhibit OSC behaviors? If so, could these oscillations be time crystals? Positive answers to these questions could pave the way for realizing dissipation-induced, heating-immune time crystals.

We address this question by theoretically unveiling the nonequilibrium steady-state phase diagram of a dissipative Heisenberg spin system, specifically one without external driving. We demonstrate the emergence of LC and chaotic steady-states, supported by spin dynamics and linear stability analysis. We characterize the LC steady states as a CTC by examining their robustness to noisy interactions and dissipation in the thermodynamic limit.

Results
System
We consider a dissipative interacting system governed by the Lindblad master equation ($\hbar = 1$),

$$\frac{d\hat{\rho}(t)}{dt} = -i[\hat{H}, \hat{\rho}(t)] + \frac{1}{2}\sum_n \mathcal{D}_n[\hat{\rho}(t)], \quad (1)$$

where $\hat{H}$ is the Hamiltonian governing the system's unitary evolution.

We consider the Hamiltonian to be the paradigmatic spin-1/2 Heisenberg XYZ model,

$$\hat{H} = \sum_{\langle mn \rangle} \hat{V}_{mn} = \sum_{\langle mn \rangle} \frac{1}{2d} \sum_{\alpha=x,y,z} J_\alpha \hat{\sigma}_m^\alpha \hat{\sigma}_n^\alpha, \quad (2)$$

where $\hat{\sigma}_n^\alpha$ is the Pauli operator for nth spin and all spins are localized in a d-dimensional cubic lattice. The nearest-neighbor spin pairs, denoted by $\langle mn \rangle$, are anisotropic interacting with strength J_α. Each spin undergoes an incoherent downward flipping process governed by

$$\mathcal{D}_n[\hat{\rho}] = \Gamma(\hat{\sigma}_n^- \hat{\rho} \hat{\sigma}_n^+ - \{\hat{\sigma}_n^+ \hat{\sigma}_n^-, \hat{\rho}\}/2), \quad (3)$$

at strength Γ, with $\hat{\sigma}_n^\pm = (\hat{\sigma}_n^x \pm i\hat{\sigma}_n^y)/2$.

These single-site dissipations break the time reversibility and other relevant symmetries of the system which usually results in the uniqueness of a stationary steady state[109–113]. As illustrated in Fig. 1a, a CTC is a nonstationary steady state characterized by a periodic oscillation in the local observable $\hat{O}$ of a time-independent many-body system, which spontaneously breaks the continuous time-translation symmetry of the system. This periodic oscillation is stabilized by many-body interactions in the thermodynamic limit, denoted by $\lim_{N\to\infty}\langle\hat{O}\hat{\rho}_{ss}(t \gg 1)\rangle = O(t) = O(t + T)$, where N is the system size and T is the period of oscillation. Moreover, the periodic oscillation is robust against small, locality-preserving perturbations to both the state and the equation of motion[68,69,114]. The above definition of CTC excludes the LC behaviors exhibited by the nonlinear systems with only a few degrees of freedom, such as a single van der Pol oscillator[115] and Belousov-Zhabotinsky reaction[116], from being considered as candidates for time crystals.

Mean-field phase diagram
To investigate the rich nonequilibrium phases in the thermodynamic limit ($N \to \infty$)[88], we conduct our study at the mean-field level which assumes that all spins are uncorrelated, meaning the system is in a product state: $\hat{\rho} \approx \otimes_{n=1}^{N\to\infty} \hat{\rho}_n$. Given the limitations of the mean field theory in one-dimensional systems[87,88], we focus on two-dimensional systems composed of infinite 3×3 clusters as illustrated in Fig. 1b. It is important to note that the cluster here refers to a unit cell in which the spins can exist in distinct states. The system is assumed to consist of an infinite number of such clusters, and the boundaries of these clusters are treated using periodic boundary conditions. In other words, we rewrite the density matrix as

$\hat{\rho} \approx \hat{\rho}_C \otimes \hat{\rho}_C \otimes \hat{\rho}_C \cdots$ with $\hat{\rho}_C = \otimes_{n=1}^{N_c}\hat{\rho}_n$ and a cluster size $N_C = 9$. Therefore, a set of $3N_c$ nonlinear Bloch equations is obtained from Eq. (1),

$$\frac{d\langle\hat{\sigma}_n^x\rangle}{dt} = -\frac{\Gamma}{2}\langle\hat{\sigma}_n^x\rangle + \sum_m \frac{J_y\langle\hat{\sigma}_n^z\rangle\langle\hat{\sigma}_m^y\rangle - J_z\langle\hat{\sigma}_n^y\rangle\langle\hat{\sigma}_m^z\rangle}{d},$$

$$\frac{d\langle\hat{\sigma}_n^y\rangle}{dt} = -\frac{\Gamma}{2}\langle\hat{\sigma}_n^y\rangle + \sum_m \frac{J_z\langle\hat{\sigma}_n^x\rangle\langle\hat{\sigma}_m^z\rangle - J_x\langle\hat{\sigma}_n^z\rangle\langle\hat{\sigma}_m^x\rangle}{d}, \quad (4)$$

$$\frac{d\langle\hat{\sigma}_n^z\rangle}{dt} = -\Gamma(\langle\hat{\sigma}_n^z\rangle + 1) + \sum_m \frac{J_x\langle\hat{\sigma}_n^y\rangle\langle\hat{\sigma}_m^x\rangle - J_y\langle\hat{\sigma}_n^x\rangle\langle\hat{\sigma}_m^y\rangle}{d},$$

where n is an index within a cluster C and the sum over m encompasses the nearest neighbors of the nth spin. Although the mean-field approach may fail in systems with short-range interactions, for the nearest-neighbor Heisenberg spin system considered in our study, we conducted precise full quantum numerical calculations on finite-size systems with periodic boundary conditions. These calculations reveal that two-body correlations significantly diminish as the system size increases (see Supplementary Note 1). This observation is consistent with the approximations inherent in mean-field methods.

Figure 2a shows the phase diagram numerically determined from spin dynamics with fixed $J_z = \gamma = 1$. The paramagnetic (PM) phase aligns all spins downward, i.e., $\langle\hat{\sigma}_n^{x(y)}\rangle = 0$, $\langle\hat{\sigma}_n^z\rangle = -1$, preserving the system's Z_2 symmetry ($\hat{\sigma}_n^x \to -\hat{\sigma}_n^x$, $\hat{\sigma}_n^y \to -\hat{\sigma}_n^y$). This Z_2 symmetry of the system is spontaneously broken in the ferromagnetic (FM) phase, where $\langle\hat{\sigma}_n^{x(y)}\rangle \neq 0$. The spin-density-wave (SDW) phase has a period greater than two lattice sites in at least one direction. The antiferromagnetic (AFM) and staggering XY (sXY) phases as found in Lee et al.[88] would emerge when the selected cluster contains an even number of spins along any axis (see Supplementary Note 2). In addition to those stationary phases, a nonstationary OSC phase, which spontaneously breaks time-translation symmetry, emerges within SDW phase region. Unlike PM and FM, which are spatially uniform phases and can exist without dissipation[88,117], SDW and OSC are spatially non-uniform states that exist only under nonequilibrium circumstances.

Those OSC steady states can be further classified into LC and chaos based on the Lyapunov exponent λ[118]. The LC steady states here are CTCs because they are characterized not only by stable periodic oscillations but also by the spontaneous breaking of continuous time-translation symmetry in many-body systems. For example, as shown in Fig. 2b, we present a detailed phase diagram of OSC phases with fixed $J_y = 1.1$, where the CTC and chaos correspond to $\lambda = 0$ and $\lambda > 0$, respectively (see details in the "Calculation of Lyapunov exponent" subsection in the "METHOD" section). In Fig. 2c–g, we demonstrate the different dynamical behaviors of FM, PM, SDW, CTC, and chaos phases by projecting the dynamic trajectories of magnetization onto the y-z plane of the Bloch sphere. The highlighted circular blocks correspond to the initial states $|\psi_n(t=0)\rangle = (|\uparrow\rangle + e^{in\pi/9}|\downarrow\rangle)/\sqrt{2}$ for the spins with $n = 1, 4, 7$ as labeled in Fig. 1b. The dynamical behaviors of magnetization $\langle\hat{\sigma}_{n=1,4,7}^{\alpha=y,z}\rangle$ illustrate that the stationary SDW phase corresponds to fixed points, while either LC attractors or chaotic behavior are observed in the nonstationary OSC phase.

The Heisenberg XXZ model is a loyal supporter of PM, where the system has isotropic interactions ($J_x = J_y$) in x-y plane, which conserve magnetization, leaving no mechanism to counteract the dissipation-induced spin downwards. In the XYZ model, the anisotropic interaction ($J_x \neq J_y$) breaks the conservation of magnetization, leading to spin fluctuation with pairs of spins flipping upwards or downwards simultaneously. This spin fluctuation also allows each spin to precess around its effective magnetic field $\overrightarrow{B}_n^{\text{eff}} = \sum_{\langle mn \rangle}(J_x\langle\hat{\sigma}_m^x\rangle, J_y\langle\hat{\sigma}_m^y\rangle, J_z\langle\hat{\sigma}_m^z\rangle)$, which originates from interactions with surrounding spins as shown in Fig. 1c. The competition between the spin fluctuation or precession and the dissipation-induced spin downwards complicates the scenario, leading to the emergence of other phases when the dissipation no longer dominates. The balanced competition results in stationary phases such as FM and SDW. This balanced

competition can also turn into cooperation under suitable parameters, giving rise to nonstationary OSC phases that break energy conservation. Those steady states can only be achieved with sufficiently strong anisotropic interactions. Therefore, assuming a sufficiently large cluster size is essential for accessing a broader range of possible steady states. Figure 1d illustrates the case that neighboring spins tend to align antiparallel, i. e., $J_{\alpha=x,y,z} > 0$ (other cases can be analyzed similarly), to illustrate the microscopic cycle of this dynamical cooperation. The system gains energy when the dissipation

flips down the nth spin. This process also would be recognized as implicit incoherent drive[49] in the sense that it helps system to gain the energy. Following is an energy-conserving process that spin fluctuations cause two neighboring spins to be in a coherent superposition of up or down simultaneously. Finally, when dissipation flips the $(n + 1)$th spin downward to align antiparallel with neighboring spins, the system releases energy.

The energy gain and loss of Floquet time crystals primarily arises from coherent driving. In driven-dissipative systems, the driving and dissipation can respectively serve as mechanisms for energy gain and loss[41–46,49–66]. Without driving, if the dissipation solely reduces the system's energy, such as photon leakage from a cavity leading to irreversible energy loss, the system would decay into a trivial steady state[58–63]. In our scenario, these microscopic cycles sustain the nonconservative OSC behavior, where dissipation plays the dual role of energy gain and loss in cooperation with anisotropic-interaction-induced spin fluctuations. Therefore, our work introduces, to the best of our knowledge, an entirely new mechanism for the emergence of CTC.

Linear stability analysis

To further confirm the time-dependent nonequilibrium phase, we introduce small local perturbations $\delta\hat{\rho}_C$ to the fixed-point solution $\hat{\rho}_C^{(0)}$ of Eq. (4), which is numerically obtained by setting the left hand side of Eq. (4) to zero. The characteristic equation of motion for $\delta\hat{\rho}_C$ is derived by linearizing the system and denoted as $\partial_t \delta\hat{\rho}_C = \mathcal{M}[\delta\hat{\rho}_C]$, where the superoperator $\mathcal{M}$ is referred to as Jacobian. Therefore, the dynamical behavior of local perturbations can be expressed as $\delta\hat{\rho}_C = \sum_j c_j e^{\lambda_j t} \delta\hat{\rho}_{C,j}$, where c_j and λ_j are the superposition coefficients and eigenvalues corresponding to the j-th eigenmode $\delta\hat{\rho}_{C,j}$ of the Jacobian. Here, eigenvalues are ordered in descending real parts, i.e., $\mathrm{Re}[\lambda_1] \geq \mathrm{Re}[\lambda_2] \geq \cdots$. Therefore, when all eigenvalues have negative real parts, $\delta\hat{\rho}_C$ will decay to zero over the system's relaxation time, indicating that the fixed-point solution $\hat{\rho}_C^{(0)}$ represents the steady state. The appearance of eigenvalues with positive real parts results in the exponential growth of the local perturbations $\delta\hat{\rho}_C$, revealing that the fixed-point solution $\hat{\rho}_C^{(0)}$ is a metastable state. In additon, the system will evolve into a time-dependent steady state if the imaginary parts are nonzero.

Figure 3a, b shows the real and imaginary parts of the first two eigenvalues, λ_1 (triangles) and λ_2 (circles), of the Jacobian $\mathcal{M}$. The phase
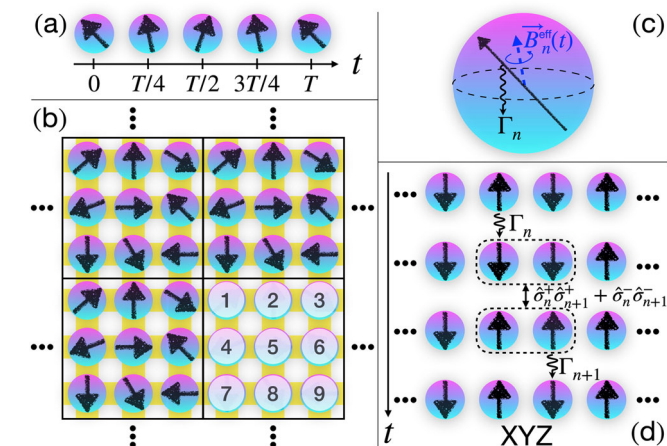

Fig. 1 | Illustration of continuous time crystals (CTCs) and their mechanism. A persistent oscillation with period T of spins in (**a**) is the core feature of the CTCs, which emerge in a two-dimensional dissipative Heisenberg spin system composed of infinite 3×3 clusters, with each spin indexed by $n \in [1, 9]$ in (**b**). As shown in (**c**), the dynamics of the nth spin are governed by the interplay between the dissipation Γ_n, which drives the spin downward, and the XYZ spin interaction, which induces an effective magnetic field $\vec{B}_n^{\mathrm{eff}}$. **d** Illustrates the mechanism of the CTCs, realized through a microscopic cycle that involves three steps: the energy loss induced by dissipation Γ_m, spin fluctuations driven by the anisotropic interaction $\hat{\sigma}_n^+ \hat{\sigma}_{n+1}^+ + \hat{\sigma}_n^- \hat{\sigma}_{n+1}^-$, and the energy gain induced by dissipation Γ_{n+1}.
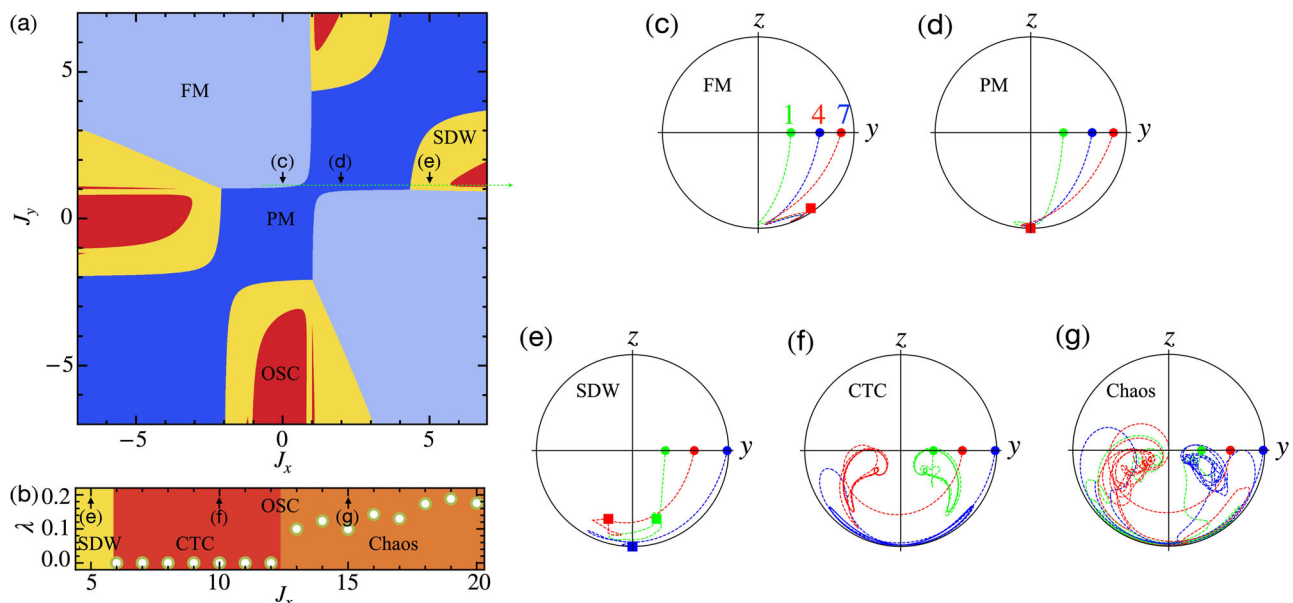

Fig. 2 | Nonequilibrium phase diagram and spin dynamics. a Shows the mean-field phase diagram with $J_z = \gamma = 1$, which includes three stationary phases: paramagnetic (PM), ferromagnetic (FM), and spin-density-wave (SDW), along with one additional nonstationary oscillatory (OSC) phase. The OSC phases can further be distinguished into continuous time crystal (CTC) and chaotic phases by calculating

the Lyapunov exponent λ, as exemplified in (**b**) with $J_y = 1.1$ (marked with the green dotted line in (**a**)). **c–g** Indicated by arrows in (**a, b**) and corresponding to $J_x = 0, 2, 5, 10,$ and 15, respectively, display the magnetization dynamic trajectories on the y-z plane for spins with $n = 1, 4, 7$ in each phase. The solid circles mark the initial states and the fixed-point fates of FM, PM, and SDW are marked with square blocks.
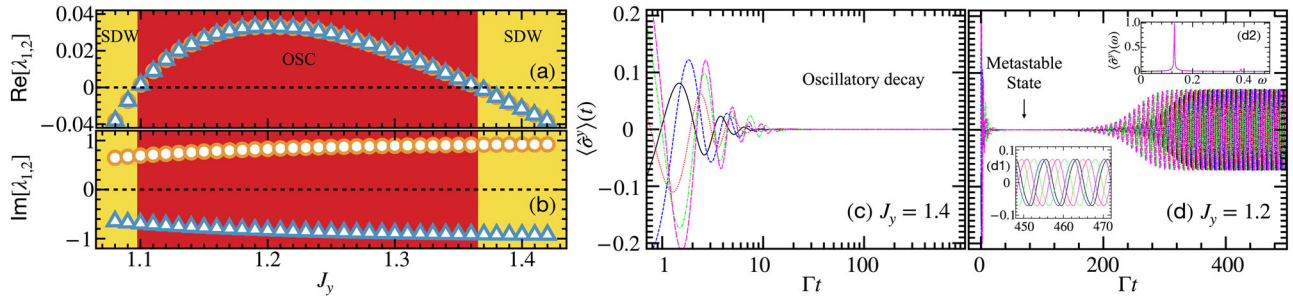
Fig. 3 | Linear stability analysis. a, b Share the same x-axis and show the real and imaginary parts of the first two eigenvalues λ_1 (triangles) and λ_2 (circles) of the Jacobian $\mathcal{M}$ with fixed $J_x = 5.9$, $J_z = \gamma = 1$. The nonzero conjugate pairs of the imaginary parts indicate oscillatory dynamics. This oscillation decays to a stationary spin-density-wave (SDW) phase when the real parts are negative, and stabilizes to a nonstationary oscillatory (OSC) phase when the real parts are positive. **c, d** Share the same y-axis and show the robustness of dynamics of $\langle \hat{\sigma}^y \rangle$ for different initial states $|\psi_n(t=0)\rangle = (|\uparrow\rangle + \sqrt{99}e^{i(r_n+c_n)\pi/k}|\downarrow\rangle)/10$ with $k = 3$ (black solid line), 6 (blue short-dashed line), 9 (red dotted line), 12 (green dot-dashed line), 15 (magenta solid line). The zoom-in plot of (**d**) and the Fourier spectrum of the selected dynamical regions ($\Gamma t \in [400, 1000]$) of (**d**) are respectively shown in (**d1** and **d2**). The dashed lines in (**a, b**) highlight zero values.
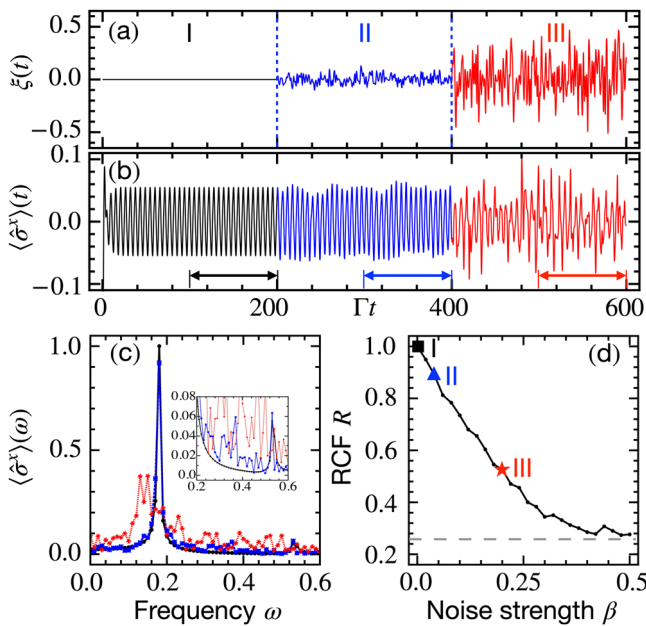

Fig. 4 | Rigidity of continuous time crystals (CTCs) under Gaussian white noise. a, b Share the x-axis and show the noisy interaction and spin dynamics with three stages: The noiseless CTC (stage I) is perturbed by weak noise (stage II) and strong noise (stage III) at $\Gamma t = 200$ and 400, respectively. The noise strengths $\beta_{\mathrm{I}} = 0$, $\beta_{\mathrm{II}} = 0.04$, $\beta_{\mathrm{III}} = 0.2$ are respectively indicated in (**d**) with square, triangle and star symbols. **c** shows the Fourier spectrum of the selected arrowed regions in (**b**), with the zoom-in inset. **d** Shows that the relative crystalline fraction (RCF) R decreases as the noise strength β increases and stabilizes at the dashed gray line, where the system may still retain some information about the CTC. Here the initial state is the same as the one used in Fig. 2(c–e), and the undisturbed interaction strengths are $J_x = 7$, $J_y = 1.5$, $J_z = 1$.

boundaries of the SDW-OSC phases, $J_y = 1.098$ and $J_y = 1.366$, where the real parts of the eigenvalues switch signs, are consistent with those shown in Fig. 2a. The imaginary parts consistently appear as nonzero conjugate pairs, suggesting that by selecting an appropriate initial state, the system will: 1) evolve into the time-independent steady state with oscillatory decay behavior in the SDW phase; 2) potentially pass through a metastable state before transitioning into a LC state in the OSC phase. Those behaviors are illustrated in Fig. 3c, d by the average magnetization of one cluster, $\langle \hat{\sigma}^{\alpha=x,y,z} \rangle = \sum_{n \in C} \langle \hat{\sigma}_n^{\alpha=x,y,z} \rangle / N_C$ with initial state $|\psi_n(t=0)\rangle = (|\uparrow\rangle + \sqrt{99}e^{i(r_n+c_n)\pi/k}|\downarrow\rangle)/10$, where r_n and c_n denote the row and column of the nth spin. In Fig. 3c, d, the lines represent results

obtained from different initial states with $k = 3, 6, 9, 12, 15$. These results demonstrate the robustness of the steady states against variations in initial conditions. Specifically, for the CTC phase, different initial states only induce a phase shift in the oscillations, as shown in Fig. 3d1, while the amplitude and frequency spectrum, as depicted in Fig. 3d2, remain unchanged.

Rigidity of continuous time crystal

The rigidity of a CTC requires its periodic OSC behavior to exhibit strong robustness against fluctuations in system parameters. Here, we consider noisy interactions given by $\tilde{J}_\alpha(t) = J_\alpha + \xi_\beta(t)$, where $\xi_\beta(t)$ represents isotropic Gaussian white noise, and its standard deviation β, acts as intensity. In Fig. 4a, we design three stages of interactions, with the corresponding dynamical behavior displayed in Fig. 4b for $\langle \hat{\sigma}^x \rangle$, and its Fourier spectrum, $\langle \hat{\sigma}^x \rangle(\omega)$, for the selected regions, shown in Fig. 4c. Without noise (stage I), the system relaxes to a LC-type oscillation, whose Fourier spectrum exhibits a sharp dominant peak at $\omega = \omega_p = 0.18$ and a small peak at $\omega \approx 3\omega_p$, indicating the emergence of a prototypical CTC. We then perturb the CTC with the weak noise of strength $\beta = 0.04$ at stage II. This perturbation has nearly no effect on the main peak, only introducing weak higher-frequency components in the Fourier spectrum as shown in the inset of Fig. 4c, indicating that the CTC is still thriving. Finally, we quench the system with much stronger white noise of strength $\beta = 0.2$ at stage III. The regular periodic oscillations are significantly altered, with the ω_p component no longer being the dominant peak, and numerous other frequency components appearing. Consequently, the CTC becomes softened under this strong noise.

Furthermore, we define the relative crystalline fraction (RCF), $R_\eta = \Omega_\eta/\Omega_{\mathrm{I}}$, to quantify the rigidity of the CTC. The crystalline fraction for stage $\eta = \mathrm{I, II, III}$ is defined as $\Omega_\eta = \sum_{\omega \in [\omega_p - \delta\omega, \omega_p + \delta\omega]} \langle \hat{\sigma}_\eta^x \rangle(\omega) / \sum_{\omega \in [0, \Delta\omega]} \langle \hat{\sigma}_\eta^x \rangle(\omega)$, with the principal frequency ω_p and its frequency width $\delta\omega$ in the noiseless case. Here $\Delta\omega$ denotes the frequency window used to calculate the crystalline fraction. We set $\delta\omega = 0.08$ and $\Delta\omega = 0.6$ for our calculations. The RCFs for the three stages are $R_{\mathrm{I}} = 1$, $R_{\mathrm{II}} = 0.89$, and $R_{\mathrm{III}} = 0.53$ as shown in Fig. 4d, where illustrates how the CTC melts as the noise strength increases. The CTC's RCF decreases as the noise increases and stabilizes at the dashed gray line, indicating that, even in the presence of strong noise, the system's OSC behavior may still retain some information about the CTC. We have also verified its robustness under other noisy interactions (see Supplementary Note 3) and noisy dissipation.

Experimental realization

We have recently experimentally implemented independent loss and gain between $|\downarrow\rangle = |F = 0, m_F = 0\rangle$ and $|\uparrow\rangle = |F = 1, m_F = 0\rangle$ states in the $^2S_{1/2}$ manifold of ^{171}Yb$^+$. This was achieved by optically pumping the ions to six auxiliary excited states and adiabatically eliminating the states exhibiting
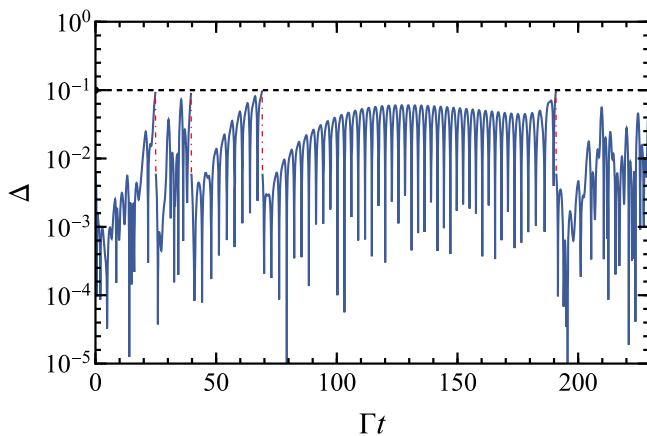
Fig. 5 | Dynamics of distance. Time evolution of the distance $\Delta(t)$ between the fiducial trajectory and auxiliary trajectory for chaotic phase. The black dashed horizontal line denotes the given threshold $\Delta_{\max} = 0.1$ for resetting the auxiliary trajectory (red dot-dashed vertical lines). Here $J_x = 13$, $J_y = 1.1$, $J_z = \gamma = 1.0$.

spontaneous emission[80]. The XYZ interactions have been realized in experiments by coupling the collective motion of ions to their internal states[119–123]. We find that the power-law decay characteristics of these interactions do not influence the existence of OSC behavior (see Supplementary Note 4). The XYZ interactions have also been proposed to be realizable through techniques such as two-photon resonance in systems such as Rydberg atoms, Rydberg-dressed atoms, and dipolar atoms or molecules[88].

Conclusions

In summary, we have proposed a CTC mechanism resulting from the competition between dissipation-induced spin downwards and anisotropic-interaction-induced spin precession or spin fluctuation. In the past, the general understanding of CTCs primarily focused on the interplay of dissipation and driving-induced quantum coherence but gave less attention to the role of interaction. Therefore, this represents, to the best of our knowledge, a completely new ergodic-breaking mechanism in which interactions play a crucial role. Since there is no external drive, the realized CTC is not subject to heating, allowing its lifetime can be as long as the system's.

This work paves the way for future explorations of CTCs that are immune to heating in other systems, including Hubbard model[99,100] and Rydberg model[95,124,125] using the methods introduced here and other numerical approaches[87,126–129] involving quantum fluctuations and correlations. The experimentally accessible CTC provides further motivation to use dissipations as resources for exploring nonequilibrium quantum dynamics, such as quantum synchronization. The existence of CTCs and chaotic phases opens a pathway to investigate reversible-to-irreversible transitions[130] in dissipative quantum systems.

Method

Calculation of Lyapunov exponent

We employ the largest Lyapunov exponent (LE), a metric introduced in ref. [118], to make discrimination between LC and chaos behavior. In analogy to the classical definition, we use two quantum trajectories, fiducial trajectory and auxiliary trajectory, to simulate the evolution of the system. Here the auxiliary trajectory is initialized as a normalized state but with a perturbation on the normalized initial fiducial state $\psi_f^{\text{ini.}}$, namely $\psi_a^{\text{ini.}} = \psi_f^{\text{ini.}} + \varepsilon\psi_{\text{ran.}}$ with the random perturbative state $\psi_{\text{ran.}}$ and $\varepsilon \ll 1$. The definition of the largest LE is based on the distance of these two trajectories and the distance is defined as difference between observables of these two trajectories. Here we choose the magnetization along y direction $\bar{\sigma}^y(t) = \frac{1}{N_C}\sum_{n \in C}\langle\psi_n(t)|\hat{\sigma}^y(t)|\psi_n(t)\rangle$ as the observable. The initial distance $\Delta(t=0) = |\bar{\sigma}_f^y(t=0) - \bar{\sigma}_a^y(t=0)|$ plays the reference during the time evolution. When the time-dependent distance

$\Delta(t) = |\bar{\sigma}_f^y(t) - \bar{\sigma}_a^y(t)|$ exceeds a given threshold $\Delta_{\max}$ at a time t_k, $\Delta(t_k)$ is reset to the initial distance $\Delta(t=0)$ through renormalizing the auxiliary trajectory close to the fiducial trajectory. Finally, the largest LE is given by

$$\lambda = \lim_{t \to \infty} \frac{1}{t}\sum_k \ln d_k, \qquad (5)$$

where k indexes each time point that the threshold $\Delta_{\max}$ is touched and $d_k = \Delta(t_k)/\Delta_0$. The fact that auxiliary trajectory respectively tends to be attracted to the fiducial state in the LC case and tends to away from the fiducial state in the chaos behavior, results in vanished LE $\lambda = 0$ and nonzero LE $\lambda \neq 0$ for LC and chaotic behavior respectively.

As shown in Fig. 5, here we consider the parameters as $J_x = 13, J_y = 1.1, J_z = \gamma = 1.0$, corresponding to the chaotic phase in the Fig. 2b of the main text. It can be observed that the dynamical distance Δ frequently touches the set threshold distance $\Delta_{\max}$ during the evolution, indicating the nonzero LE $\lambda = 0.1$ for the corresponding chaotic scenario.

Data availability

The data that support the plots within this paper and other findings of this study are available from the authors upon reasonable request.

Code availability

The computer codes that support the calculations within this paper are available upon reasonable request via email to S. Yang or J. Jie.

References

1. Shapere, A. & Wilczek, F. Classical time crystals. *Phys. Rev. Lett.* **109**, 160402 (2012).
2. Wilczek, F. Quantum time crystals. *Phys. Rev. Lett.* **109**, 160401 (2012).
3. Li, T. et al. Space-time crystals of trapped ions. *Phys. Rev. Lett.* **109**, 163001 (2012).
4. Zakrzewski, J. Crystals of time. *Physics* **5**, 116 (2012).
5. Bruno, P. Impossibility of spontaneously rotating time crystals: A no-go theorem. *Phys. Rev. Lett.* **111**, 070402 (2013).
6. Nozières, P. Time crystals: Can diamagnetic currents drive a charge density wave into rotation? *Europhys. Lett.* **103**, 57008 (2013).
7. Watanabe, H. & Oshikawa, M. Absence of quantum time crystals. *Phys. Rev. Lett.* **114**, 251603 (2015).
8. Kozin, V. K. & Kyriienko, O. Quantum Time Crystals from Hamiltonians with Long-Range Interactions. *Phys. Rev. Lett.* **123**, 210602 (2019).
9. Sacha, K. Modeling spontaneous breaking of time-translation symmetry. *Phys. Rev. A* **91**, 033617 (2015).
10. Khemani, V. et al. Phase structure of driven quantum systems. *Phys. Rev. Lett.* **116**, 250401 (2016).
11. von Keyserlingk, C. W., Khemani, V. & Sondhi, S. L. Absolute stability and spatiotemporal long-range order in Floquet systems. *Phys. Rev. B* **94**, 085112 (2016).
12. Else, D. V., Bauer, B. & Nayak, C. Floquet time crystals. *Phys. Rev. Lett.* **117**, 090402 (2016).
13. Yao, N. Y. et al. Discrete time crystals: Rigidity, criticality, and realizations. *Phys. Rev. Lett.* **118**, 030401 (2017).
14. Richerme, P. How to create a time crystal. *Physics* **10**, 5 (2017).
15. Russomanno, A., Iemini, F., Dalmonte, M. & Fazio, R. Floquet time crystal in the Lipkin-Meshkov-Glick model. *Phys. Rev. B* **95**, 214307 (2017).
16. Surace, F. M. et al. Floquet time crystals in clock models. *Phys. Rev. B* **99**, 104303 (2019).
17. Sakurai, A. et al. Chimera time-crystalline order in quantum spin networks. *Phys. Rev. Lett.* **126**, 120606 (2021).

Article

18. Pal, S., Nishad, N., Mahesh, T. S. & Sreejith, G. J. Temporal order in periodically driven spins in star-shaped clusters. *Phys. Rev. Lett.* **120**, 180602 (2018).

19. Else, D. V., Monroe, C., Nayak, C. & Yao, N. Y. Discrete time crystals. *Annu. Rev. Condens. Matter Phys.* **11**, 467–499 (2020).

20. Xu, P. & Deng, T.-S. Boundary discrete time crystals induced by topological superconductors in solvable spin chains. *Phys. Rev. B* **107**, 104301 (2023).

21. Chen, T., Shen, R., Lee, C. H., Yang, B. & Bomantara, R. W. A robust large-period discrete time crystal and its signature in a digital quantum computer. *arXiv* https://arxiv.org/abs/2309.11560 (2023).

22. Rovny, J., Blum, R. L. & Barrett, S. E. Observation of discrete-time-crystal signatures in an ordered dipolar many-body system. *Phys. Rev. Lett.* **120**, 180603 (2018).

23. Rovny, J., Blum, R. L. & Barrett, S. E. ^{31}P NMR study of discrete time-crystalline signatures in an ordered crystal of ammonium dihydrogen phosphate. *Phys. Rev. B* **97**, 184301 (2018).

24. Choi, S. et al. Observation of discrete time-crystalline order in a disordered dipolar many-body system. *Nature* **543**, 221–225 (2017).

25. Zhang, J. et al. Observation of a discrete time crystal. *Nature* **543**, 217–220 (2017).

26. Kyprianidis, A. et al. Observation of a prethermal discrete time crystal. *Science* **372**, 1192–1196 (2021).

27. Mi, X. et al. Time-crystalline eigenstate order on a quantum processor. *Nature* **601**, 531–536 (2022).

28. Else, D. V., Bauer, B. & Nayak, C. Prethermal phases of matter protected by time-translation symmetry. *Phys. Rev. X* **7**, 011026 (2017).

29. Mori, T. Floquet prethermalization in periodically driven classical spin systems. *Phys. Rev. B* **98**, 104303 (2018).

30. Ye, B., Machado, F. & Yao, N. Y. Floquet phases of matter via classical prethermalization. *Phys. Rev. Lett.* **127**, 140603 (2021).

31. Pizzi, A., Nunnenkamp, A. & Knolle, J. Classical prethermal phases of matter. *Phys. Rev. Lett.* **127**, 140602 (2021).

32. Randall, J. et al. Many-body-localized discrete time crystal with a programmable spin-based quantum simulator. *Science* **374**, 1474–1478 (2021).

33. Verstraete, F., Wolf, M. M. & Cirac, J. I. Quantum computation and quantum-state engineering driven by dissipation. *Nature Phys.* **5**, 633–636 (2009).

34. Poyatos, J. F., Cirac, J. I. & Zoller, P. Quantum reservoir engineering with laser cooled trapped ions. *Phys. Rev. Lett.* **77**, 4728–4731 (1996).

35. Preskill, J. The physics of quantum information. *arXiv* https://arxiv.org/abs/2208.08064 (2022).

36. Lin, Y. et al. Dissipative production of a maximally entangled steady state of two quantum bits. *Nature* **504**, 415–418 (2013).

37. Shankar, S. et al. Autonomously stabilized entanglement between two superconducting quantum bits. *Nature* **504**, 419–422 (2013).

38. Magnard, P. et al. Fast and unconditional all-microwave reset of a superconducting qubit. *Phys. Rev. Lett.* **121**, 060502 (2018).

39. Malinowski, M. et al. Generation of a maximally entangled state using collective optical pumping. *Phys. Rev. Lett.* **128**, 080503 (2022).

40. Liu, Y., Wang, Z., Yang, C., Jie, J. & Wang, Y. Dissipation-induced extended-localized transition. *Phys. Rev. Lett.* **132**, 216301 (2024).

41. Gong, Z. & Ueda, M. Time Crystals in Open Systems. *Physics* **14**, 104 (2021).

42. Gong, Z., Hamazaki, R. & Ueda, M. Discrete time-crystalline order in cavity and circuit QED systems. *Phys. Rev. Lett.* **120**, 040404 (2018).

43. Zhu, B. et al. Dicke time crystals in driven-dissipative quantum many-body systems. *New J. Phys.* **21**, 073028 (2019).

44. Lazarides, A., Roy, S., Piazza, F. & Moessner, R. Time crystallinity in dissipative Floquet systems. *Phys. Rev. Res.* **2**, 022002(R) (2020).

45. Riera-Campeny, A., Moreno-Cardoner, M. & Sanpera, A. Time crystallinity in open quantum systems. *Quantum* **4**, 270 (2020).

46. Sakurai, A., Bastidas, V. M., Estarellas, M. P., Munro, W. J. & Nemoto, K. Dephasing-induced growth of discrete time-crystalline order in spin networks. *Phys. Rev. B* **104**, 054304 (2021).

47. Buča, B. & Jaksch, D. Dissipation induced nonstationarity in a quantum gas. *Phys. Rev. Lett.* **123**, 260401 (2019).

48. Buča, B., Tindall, J. & Jaksch, D. Non-stationary coherent quantum many-body dynamics through dissipation. *Nature Commun.* **10**, 1730 (2019).

49. Minganti, F., Arkhipov, I. I., Miranowicz, A. & Nori, F. Correspondence between dissipative phase transitions of light and time crystals. *arXiv*, https://arxiv.org/abs/2008.08075 (2020).

50. Hajdušek, M. et al. Seeding crystallization in time. *Phys. Rev. Lett.* **128**, 080603 (2022).

51. Krishna, M. et al. Measurement-induced continuous time crystals. *Phys. Rev. Lett.* **130**, 150401 (2023).

52. Keßler, H. et al. Emergent limit cycles and time crystal dynamics in an atom-cavity system. *Phys. Rev. A* **99**, 053605 (2019).

53. Tucker, K. et al. Shattered time: can a dissipative time crystal survive many-body correlations? *N. J. Phys.* **20**, 123003 (2018).

54. Lledó, C., Mavrogordatos, T. K. & Szymańska, M. H. Driven Bose-Hubbard dimer under nonlocal dissipation: A bistable time crystal. *Phys. Rev. B* **100**, 054303 (2019).

55. Seibold, K., Rota, R. & Savona, V. Dissipative time crystal in an asymmetric nonlinear photonic dimer. *Phys. Rev. A* **101**, 033839 (2020).

56. Prazeres, L. F. D., Souza, L. D. S. & Iemini, F. Boundary time crystals in collective *d*-level systems. *Phys. Rev. B* **103**, 184308 (2021).

57. Iemini, F. et al. Boundary time crystals. *Phys. Rev. Lett.* **121**, 035301 (2018).

58. Keßler, H. et al. Observation of a dissipative time crystal. *Phys. Rev. Lett.* **127**, 043602 (2021).

59. Kongkhambut, P. et al. Realization of a periodically driven open three-level Dicke model. *Phys. Rev. Lett.* **127**, 253601 (2021).

60. Kongkhambut, P. et al. Observation of a continuous time crystal. *Science* **377**, 670–673 (2022).

61. Dogra, N. et al. Dissipation-induced structural instability and chiral dynamics in a quantum gas. *Science* **366**, 1496–1499 (2019).

62. Zupancic, P. et al. *P*-band induced self-organization and dynamics with repulsively driven ultracold atoms in an optical cavity. *Phys. Rev. Lett.* **123**, 233601 (2019).

63. Dreon, D. et al. Self-oscillating pump in a topological dissipative atom-cavity system. *Nature* **608**, 494–498 (2022).

64. Taheri, H. et al. All-optical dissipative discrete time crystals. *Nat. Commun.* **13**, 848 (2022).

65. Autti, S., Eltsov, V. B. & Volovik, G. E. Observation of a time quasicrystal and its transition to a superfluid time crystal. *Phys. Rev. Lett.* **120**, 215301 (2018).

66. Kreil, A. J. E. et al. Tunable space-time crystal in room-temperature magnetodielectrics. *Phys. Rev. B* **100**, 020406(R) (2019).

67. Sacha, K. & Zakrzewski, J. Time crystals: A review. *Rep. Prog. Phys.* **81**, 016401 (2017).

68. Khemani, V., Moessner, R. & Sondhi, S. L. A brief history of time crystals. *arXiv*, https://arxiv.org/abs/1910.10745 (2019).

69. Zaletel, M. P. et al. Colloquium: Quantum and classical discrete time crystals. *Rev. Mod. Phys.* **95**, 031001 (2023).

70. Guo, L. & Liang, P. Condensed matter physics in time crystals. *New J. Phys.* **22**, 075003 (2020).

71. Strogatz, S. H. *Nonlinear Dynamics and Chaos: With Applications to Physics, Biology, Chemistry, and Engineering* https://books.google.com.hk/books?id=1kpnDwAAQBAJ (CRC Press, 2018).

72. Kasis, A., Monshizadeh, N. & Lestas, I. Primary frequency regulation in power grids with on-off loads: Chattering, limit cycles and convergence to optimality. *Automatica* **131**, 109736 (2021).

73. Gonze, D. Modeling circadian clocks: Roles, advantages, and limitations. *Open Life Sci.* **6**, 712–729 (2011).

74. Lörch, N. et al. Quantum synchronization blockade: Energy quantization hinders synchronization of identical oscillators. *Phys. Rev. Lett.* **118**, 243602 (2017).

75. Nigg, S. E. Observing quantum synchronization blockade in circuit quantum electrodynamics. *Phys. Rev. A* **97**, 013811 (2018).

76. Roulet, A. & Bruder, C. Synchronizing the smallest possible system. *Phys. Rev. Lett.* **121**, 053601 (2018).

77. Koppenhöfer, M. & Roulet, A. Optimal synchronization deep in the quantum regime: Resource and fundamental limit. *Phys. Rev. A* **99**, 043804 (2019).

78. Laskar, A. W. et al. Observation of quantum phase synchronization in spin-1 atoms. *Phys. Rev. Lett.* **125**, 013601 (2020).

79. Parra-López, Á. & Bergli, J. Synchronization in two-level quantum systems. *Phys. Rev. A* **101**, 062104 (2020).

80. Zhang, L. et al. Quantum synchronization of a single trapped-ion qubit. *Phys. Rev. Res.* **5**, 033209 (2023).

81. Wang, Z. et al. Absence of correlations in dissipative interacting qubits: a no-go theorem. *Phys. Rev. B* **110**, 155129 (2024).

82. Nie, X. & Zheng, W. Mode softening in time-crystalline transitions of open quantum systems. *Phys. Rev. A* **107**, 033311 (2023).

83. Breuer, H. P., Petruccione, F. & Petruccione, S. P. A. P. F. *The Theory of Open Quantum Systems* https://books.google.com.hk/books?id=0Yx5VzaMYm8C (Oxford University Press, 2002).

84. Rivas, Á. & Huelga, S. F. *Open Quantum Systems: An Introduction* https://books.google.com.hk/books?id=FGCuYsIZAA0C (Springer Berlin Heidelberg, 2011).

85. de Vega, I. & Alonso, D. Dynamics of non-Markovian open quantum systems. *Rev. Mod. Phys.* **89**, 015001 (2017).

86. Weimer, H., Kshetrimayum, A. & Orús, R. Simulation methods for open quantum many-body systems. *Rev. Mod. Phys.* **93**, 015008 (2021).

87. Jin, J. et al. Cluster mean-field approach to the steady-state phase diagram of dissipative spin systems. *Phys. Rev. X* **6**, 031011 (2016).

88. Lee, T. E., Gopalakrishnan, S. & Lukin, M. D. Unconventional magnetism via optical pumping of interacting spin systems. *Phys. Rev. Lett.* **110**, 257204 (2013).

89. Jin, J., Rossini, D., Fazio, R., Leib, M. & Hartmann, M. J. Photon solid phases in driven arrays of nonlinearly coupled cavities. *Phys. Rev. Lett.* **110**, 163605 (2013).

90. Le Boité, A., Orso, G. & Ciuti, C. Steady-state phases and tunneling-induced instabilities in the driven dissipative Bose-Hubbard model. *Phys. Rev. Lett.* **110**, 233601 (2013).

91. Fitzpatrick, M. et al. Observation of a dissipative phase transition in a one-dimensional circuit QED lattice. *Phys. Rev. X* **7**, 011016 (2017).

92. Song, L. & Jin, J. Crossover from discontinuous to continuous phase transition in a dissipative spin system with collective decay. *Phys. Rev. B* **108**, 054302 (2023).

93. Zhang, Y. & Barthel, T. Criticality and phase classification for quadratic open quantum many-body systems. *Phys. Rev. Lett.* **129**, 120401 (2022).

94. Li, Z. et al. Dissipative phase transition with driving-controlled spatial dimension and diffusive boundary conditions. *Phys. Rev. Lett.* **128**, 093601 (2022).

95. Kazemi, J. & Weimer, H. Driven-dissipative Rydberg blockade in optical lattices. *Phys. Rev. Lett.* **130**, 163601 (2023).

96. Li, Y., Li, X. & Jin, J. Quantum nonstationary phenomena of spin systems in collision models. *Phys. Rev. A* **107**, 042205 (2023).

97. Haga, T. Spontaneous symmetry breaking in nonsteady modes of open quantum many-body systems. *Phys. Rev. A* **107**, 052208 (2023).

98. Lee, T. E., Haffner, H. & Cross, M. C. Antiferromagnetic phase transition in a nonequilibrium lattice of Rydberg atoms. *Phys. Rev. A* **84**, 031402(R) (2011).

99. Wilson, R. M. et al. Collective phases of strongly interacting cavity photons. *Phys. Rev. A* **94**, 033801 (2016).

100. Schiró, M. et al. Exotic attractors of the nonequilibrium Rabi-Hubbard model. *Phys. Rev. Lett.* **116**, 143603 (2016).

101. Parmee, C. D. & Cooper, N. R. Phases of driven two-level systems with nonlocal dissipation. *Phys. Rev. A* **97**, 053616 (2018).

102. Parmee, C. D. & Cooper, N. R. Steady states of a driven dissipative dipolar XXZ chain. *J. Phys. B At. Mol. Opt. Phys.* **53**, 135302 (2020).

103. Qian, J., Dong, G., Zhou, L. & Zhang, W. Phase diagram of Rydberg atoms in a nonequilibrium optical lattice. *Phys. Rev. A* **85**, 065401 (2012).

104. Owen, E. T., Jin, J., Rossini, D., Fazio, R. & Hartmann, M. J. Quantum correlations and limit cycles in the driven-dissipative Heisenberg lattice. *New J. Phys.* **20**, 045004 (2018).

105. Chan, C.-K., Lee, T. E. & Gopalakrishnan, S. Limit-cycle phase in driven-dissipative spin systems. *Phys. Rev. A* **91**, 051601(R) (2015).

106. Li, X., Li, Y. & Jin, J. Synchronization of persistent oscillations in spin systems with nonlocal dissipation. *Phys. Rev. A* **107**, 032219 (2023).

107. Passarelli, G., Lucignano, P., Fazio, R. & Russomanno, A. Dissipative time crystals with long-range Lindbladians. *Phys. Rev. B* **106**, 224308 (2022).

108. Bunkov, Y. M. & Volovik, G. E. Spin superfluidity and magnon BEC. *arXiv*, https://arxiv.org/abs/1003.4889 (2010).

109. Evans, D. E. Irreducible quantum dynamical semigroups. *Commun. Math. Phys.* **54**, 293–297 (1977).

110. Frigerio, A. Quantum synchronization and entanglement generation. *Commun. Math. Phys.* **63**, 269 (1978).

111. Prosen, T. Comments on a boundary-driven open XXZ chain: Asymmetric driving and uniqueness of steady states. *Physica Scripta* **86**, 058511 (2012).

112. Prosen, T. Matrix product solutions of boundary driven quantum chains. *J. Phys. A: Math. Theor.* **48**, 373001 (2015).

113. Schirmer, S. G. & Wang, X. Stabilizing open quantum systems by Markovian reservoir engineering. *Phys. Rev. A* **81**, 062306 (2010).

114. Khemani, V., von Keyserlingk, C. W. & Sondhi, S. L. Defining time crystals via representation theory. *Phys. Rev. B* **96**, 115127 (2017).

115. Pikovsky, A. et al. *Synchronization: A Universal Concept in Nonlinear Sciences* (Cambridge University Press, 2001).

116. Enns, R. H. & McGuire, G. C. *Nonlinear Physics with Maple for Scientists and Engineers* (Birkhäuser, 2012).

117. Sachdev, S. *Quantum Phase Transitions* 2nd ed. https://doi.org/10.1017/CBO9780511973765 (Cambridge University Press, 2011).

118. Yusipov, I. I. et al. Quantum Lyapunov exponents beyond continuous measurements. *Chaos* **29**, 063130 (2019).

119. Debnath, S. et al. Demonstration of a small programmable quantum computer with atomic qubits. *Nature* **536**, 63–66 (2016).

120. Kranzl, F. et al. Observation of magnon bound states in the long-range, anisotropic Heisenberg model. *Phys. Rev. X* **13**, 031017 (2023).

121. Lu, Y. et al. Global entangling gates on arbitrary ion qubits. *Nature* **572**, 363–367 (2019).

122. Monroe, C. et al. Programmable quantum simulations of spin systems with trapped ions. *Rev. Mod. Phys.* **93**, 025001 (2021).

123. Zhang, J. et al. Observation of a many-body dynamical phase transition with a 53-qubit quantum simulator. *Nature* **551**, 601–604 (2017).

124. Nill, C., Brandner, K., Olmos, B., Carollo, F. & Lesanovsky, I. Many-body radiative decay in strongly interacting Rydberg ensembles. *Phys. Rev. Lett.* **129**, 243202 (2022).

125. Gambetta, F. M., Carollo, F., Marcuzzi, M., Garrahan, J. P. & Lesanovsky, I. Discrete time crystals in the absence of manifest symmetries or disorder in open quantum systems. *Phys. Rev. Lett.* **122**, 015701 (2019).

126. Schollwöck, U. The density-matrix renormalization group. *Rev. Mod. Phys.* **77**, 259–315 (2005).

127. Cui, J., Cirac, J. I. & Bañuls, M. C. Variational matrix product operators for the steady state of dissipative quantum systems. *Phys. Rev. Lett.* **114**, 220601 (2015).
128. Rota, R. et al. Quantum critical regime in a quadratically driven nonlinear photonic lattice. *Phys. Rev. Lett.* **122**, 110405 (2019).
129. Finazzi, S. et al. Corner-space renormalization method for driven-dissipative two-dimensional correlated systems. *Phys. Rev. Lett.* **115**, 080604 (2015).
130. Reichhardt, C. et al. Reversible to irreversible transitions in periodic driven many-body systems and future directions for classical and quantum systems. *Phys. Rev. Res.* **5**, 021001 (2023).

Author contributions
J. Jie initiated this project. S. Yang carried out the theoretical derivations and numerical simulations. Z. Wang provided support for the numerical techniques. J. Jie and L. Fu took on advisory roles. All authors contributed to the discussion and writing of the manuscript.

Competing interests
The authors declare no competing interests.

Additional information
Supplementary information The online version contains supplementary material available at https://doi.org/10.1038/s42005-025-02040-1.

Correspondence and requests for materials should be addressed to Libin Fu or Jianwen Jie.

Peer review information *Communications Physics* thanks the anonymous, reviewer(s) for their contribution to the peer review of this work. A peer review file is available.

Reprints and permissions information is available at http://www.nature.com/reprints

Publisher's note Springer Nature remains neutral with regard to jurisdictional claims in published maps and institutional affiliations.